Ann. Geophysicae 17, 1503–1512 (1999) © EGS – Springer-Verlag 1999

Annales Geophysicae

EDI convection measurements at 5–6 R_E in the post-midnight region

J. M. Quinn[1], G. Paschmann[2], N. Sckopke[2], V. K. Jordanova[1], H. Vaith[2], O. H. Bauer[2], W. Baumjohann[2], W. Fillius[3], G. Haerendel[2], S. S. Kerr[3], C. A. Kletzing[4], K. Lynch[1], C. E. McIlwain[3], R. B. Torbert[1], E. C. Whipple[5]

[1] Space Science Center, Morse Hall, University of New Hampshire, Durham, NH, 03824, USA
[2] Max-Planck-Institut f. extraterrestrische Physik, 85740 Garching, Germany
[3] Center for Astrophysics and Space Sciences, University of California, San Diego, La Jolla, CA, 92093, USA
[4] Department of Physics and Astronomy, University of Iowa, Iowa City, IO, 52242, USA
[5] Geophysics Program, University of Washington, Seattle, WA, 98195, USA

Received: 8 March 1999 / Revised: 10 May 1999 / Accepted: 12 May 1999

Abstract. We present the first triangulation measurements of electric fields with the electron drift instrument (EDI) on Equator-S. We show results from five high-data-rate passes of the satellite through the near-midnight equatorial region, at geocentric distances of approximately 5–6 R_E, during geomagnetically quiet conditions. In a co-rotating frame of reference, the measured electric fields have magnitudes of a few tenths of mV/m, with the $\mathbf{E} \times \mathbf{B}$ drift generally directed sunward but with large variations. Temporal variations of the electric field on time scales of several seconds to minutes are large compared to the average magnitude. Comparisons of the "DC" baseline of the EDI-measured electric fields with the mapped Weimer ionospheric model and the Rowland and Wygant CRRES measurements yield reasonable agreement.

Key words. Magnetospheric physics (electric fields; plasma convection; instruments and techniques)

1 Introduction

The electron drift instrument (EDI) was developed for the Cluster mission with the objective of measuring electric fields over a large range of plasma, magnetic-field, and electric-field regimes (Paschmann *et al.*, 1998). Because the instrument incorporated complex, closed-loop control algorithms and several newly developed hardware components, its first flight on Equator-S provided an extremely valuable opportunity to obtain experience with its operation and to verify its measurement capabilities.

One of the many goals for EDI was to provide an accurate and sensitive measurement of the highly variable convection electric fields in the key region near geosynchronous orbit, where plasma is injected into the inner magnetosphere. Despite the importance of this region to plasma transport and energization, the development of a reliable, empirically based model of electric fields has been challenging for several reasons. The typical electric field magnitude is relatively small; the plasma conditions are highly variable; and there have been only a limited number of spacecraft instrumented to make sufficiently sensitive electric-field measurements in this part of the magnetosphere. Average convection electric fields based on large data-sets have been obtained using several approaches. McIlwain (1972) derived an inner-magnetosphere electric-field model from analysis of detailed convection features seen in plasma data at different local times near geosynchronous orbit. Maynard *et al.* (1983) used a year of ISEE-1 double-probe measurements to determine average field maps at various geomagnetic activity levels. Measurements by the GEOS-2 beam experiment were analyzed by Baumjohann *et al.* (1985) and Baumjohann and Haerendel (1985) to study dependencies of the convection field at 6.6 R_E as a function of geomagnetic activity and solar-wind conditions. Recently Rowland and Wygant (1998) have published a study of convection fields as a function of K_p for $L < 8.5$ using CRRES double-probe measurements from a 10-month period. In addition to the models based on equatorial measurements, ionospheric models have been developed that, in many instances, can be mapped to the equatorial region (e.g., Weimer, 1995, 1996).

We present equatorial measurements by EDI in the near-midnight region at 5–6 R_E, during five high-data-rate passes of the satellite during late March and April, 1998. This location provides a good test of the instrument's ability to measure sensitively the weak electric fields of convection and waves.

2 Measurement technique

The electron drift instrument measures the electron drift velocity by detecting the displacement of two electron

Correspondence to: J. Quinn
E-mail: jack.quinn@unh.edu

beams fired perpendicular to the ambient magnetic field. (The drift velocity is usually dominated by the $\mathbf{E}\times\mathbf{B}$ drift, however the $\nabla\mathbf{B}$ drift can also be important). The beams are fired by a pair of electron guns and detected after one (or more) gyro orbit(s). The instrument uses two complementary techniques to measure the electron drift. In the "triangulation" technique the firing directions of the electron beams are used to determine the electron drift velocity, as described later. In this study we rely exclusively on the triangulation technique. The second technique, based on measuring differences in the times-of-flight of the two electron beams, is described in the companion work by Paschmann *et al.* (1999).

The EDI triangulation technique is based on measuring the distortion of the electron's gyro orbit by the electric field. In a uniform magnetic field with no other forces acting, an electron fired in any direction perpendicular to the ambient magnetic field **B** will execute a circular gyro orbit and return to its starting point. In the presence of a transverse electric field **E**, the trajectories are distorted and the electrons no longer return to their starting position after one gyro period. Specifically, all electrons starting at a particular location will be displaced by the same amount in one gyro period due to the $\mathbf{E}\times\mathbf{B}$ drift. This displacement is independent of the electrons' energy and original direction of travel, as neither the $\mathbf{E}\times\mathbf{B}$ drift velocity nor the gyro period depend on energy. We define the *drift step*, **d**, to be the net displacement during a single gyro period, T_g, due to a drift velocity, $\mathbf{V}_d$.

$$\mathbf{d} = \mathbf{V}_d T_g.$$

A measurement of the drift step, together with knowledge of the gyro period, is thus equivalent to measuring the drift velocity. EDI used this relationship to determine the drift velocity by measuring the drift step, using a weak beam of electrons as test particles.

The EDI triangulation technique is illustrated conceptually by Fig. 1 in the plane perpendicular to **B** (the "$\mathbf{B}_\perp$ plane"). There are two electron guns, with a detector (Det) located halfway between. The beams are represented by the dashed and dotted lines. The magnitude and orientation of the drift step, **d**, are specified by the ambient fields as described above. We have drawn **d** with its head positioned at the detector. The electron gyro radius is very large (≥1 km) compared to the scale of the figure (~1 m), and so the gyro trajectories of the beams appear as nearly straight lines. By definition, any 90°-pitch-angle electron originating at the tail-end of **d** will be displaced by the drift velocity and will hit the detector exactly one gyro period later. Therefore, an electron beam aimed so that the electrons pass through the tail of **d** will return to hit the detector after one gyro orbit. We thus call the tail of **d** the "target". Electrons fired in other directions, and not passing through the target position, will not hit the detector, except for those fired in the opposite direction, which also have a virtual source at the tail of **d**. When the guns are aimed in the unique directions that allow their beams to hit the detector after one gyro orbit, one can determine from triangulation the beam intersection

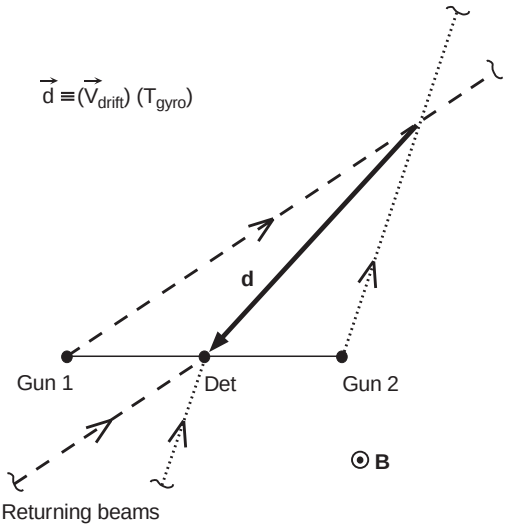

Fig. 1. Triangulation geometry for determining the drift-step vector **d**. Firing directions of the two guns (*dashed* and *dotted lines*) locate the tail of **d** when the guns are aimed so that after one gyro orbit the beams return to the detector (*Det*). The gyro radius is large compared to the figure, so the beam trajectories appear as *straight lines* on this scale

point, which corresponds to the tail of **d**. Using the known locations of the guns and detector, one can then calculate the vector **d**. Together with knowledge of the gyro period, this measurement of **d** determines the drift velocity of the electrons.

The EDI gun-detector configuration on Equator-S is different from that shown in Fig. 1, but it is geometrically equivalent. There are two gun-detector units (GDUs), mounted on opposite sides of the spacecraft and having oppositely directed fields-of-view. Each gun is capable of firing its beam in any direction within somewhat more than a full hemisphere, at polar angles up to 96°, to an accuracy of better than 1°. Similarly, each detector is able to detect electrons coming from any selected direction within a hemispherical field of view for polar angles up to 100°. The beam fired by each gun is received by the detector on the opposite side of the spacecraft. Thus, for the purposes of triangulation, the baseline separating a gun and its corresponding detector is the spacecraft diameter projected into the $\mathbf{B}_\perp$ plane. At any instant, one gun fires at a detector that is displaced from it in the $\mathbf{B}_\perp$ plane by a baseline **b**, while the other fires at a detector displaced by $-\mathbf{b}$. Therefore the configuration is geometrically identical to that shown in Fig. 1, with the two guns separated from the detector by equal distances in opposite directions. Each gun is separated from its detector on the opposite side of the spacecraft by equal and oppositely directed vectors. This is equivalent to having the two guns equidistant from a centrally located detector, as illustrated in Fig. 1. For the purposes of displaying triangulation data we will continue to use this picture, i.e., two guns and a single "virtual detector" located halfway between, at a distance of one spacecraft diameter from each gun. The triangulation baseline, formed by the projection of the gun-detector separation vectors in the $\mathbf{B}_\perp$ plane, varies with the orientation of the ambient magnetic field and spacecraft spin phase.

The technical implementation of EDI is described in detail by Paschmann *et al.* (1997, 1998). The key elements for the present study are the beam firing angles of the guns, the beam recognition by the detector, and the beam acquisition and tracking algorithms which allow sufficiently frequent "hits" to make good triangulation measurements. The angles in the triangulation measurement are taken from the gun firing directions, which are calibrated prior to launch over the entire gun solid angle. Since the beam can only return to the spacecraft if it is fired within approximately 1 degree (the beam width) of the $\mathbf{B}_\perp$ plane, we can check and update these calibrations in orbit by analyzing the distribution of beam hits over the gun solid angle for various magnetic field orientations. On Equator-S, we found that the guns' ground calibrations were preserved extremely well throughout the mission lifetime.

Each EDI gun-detector pair independently acquires and tracks the target by controlling the gun firing directions with a flexible, onboard servo algorithm. Equator-S employed a 1 keV beam energy; however the instrument is designed to use 500 eV beams also. In order to measure the electrons' time-of-flight, and to help discriminate against the background flux of ambient electrons, the beams are amplitude-modulated by a 15-chip pseudo-noise code, and the detected counts are processed by a 15-channel correlator (Vaith *et al.*, 1998). To acquire the target, the beam firing-direction is stepped at a constant angular rate in the $\mathbf{B}_\perp$ plane until the beam-recognition algorithm records a hit by comparing counts in the various correlator channels. When the beam is detected, the onboard tracking algorithm reverses the angular stepping direction so that the beam is swept repeatedly back and forth across the target direction.

The accuracy with which one can determine the drift step through triangulation depends on several factors, including the knowledge of the beam firing direction and the relative magnitude and orientation of the gun-detector baseline **b**, projected into the $\mathbf{B}_\perp$ plane, with respect to the drift step, **d**. In general, triangulation is most accurate when the baseline is comparable in magnitude to the drift step. However, with firing angles known to 1° the drift steps can be measured to better than 20% over a satisfactory dynamic range to cover inner-magnetospheric drifts. When drift steps are a few tens of times larger than the baseline, the drift direction is known accurately, but the magnitude obtained by triangulation becomes increasingly uncertain. In this large-**d** regime, the time-of-flight technique is preferred (see Paschmann *et al.*, 1999).

The EDI technique has the advantage that it is essentially geometrical in nature, and thus the absolute accuracy can be quite high. While the complexities of beam acquisition and tracking are challenging, once the return beams are detected the resulting triangulation yields a rather unambiguous result. For a given baseline and drift step orientation, the error analysis arising from uncertainties in the beam firing directions is straightforward.

The electron beam triangulation technique was first developed by the group at MPE, and flown on the GEOS-2 satellite (Melzner *et al.*, 1978). While the GEOS experiment clearly established the viability of the measurement technique, its time resolution was limited to the 6-s spacecraft spin period, and its beam deflection capability was restricted to a narrow range of magnetic-field orientations. The EDI instrument for the Cluster and Equator-S missions was developed to remove these limitations as well as to incorporate the time-of-flight technique and other improvements that would be necessary to accommodate the wide range of anticipated magnetic fields, electric fields, and ambient (background) electron fluxes.

Figure 2 illustrates the relationship between the relevant physical parameters for EDI as a function of ambient magnetic field (abscissa) and the $\mathbf{E} \times \mathbf{B}$ drift velocity (ordinate). Lines of constant electric field, from 0.01–100 mV/m, run diagonally from lower right to upper left, while lines of constant drift step, from 1 cm to 1 km, are orthogonal to these. The constant-drift-step lines also correspond to lines of constant Δt: the difference in the transit times of the two beams and the basis of the time-of-flight technique discussed in the companion study (Paschmann *et al.*, 1999). The triangulation technique is most accurate for drift steps between approximately 0.1 m and 20 m. The electric field magnitudes corresponding to this range depends upon the magnitude of **B**, as shown in Fig. 2. For larger drift steps, Δt becomes proportionally larger and the time-of-flight technique becomes more accurate. For the region of space covered in this work drift steps in the satellite frame of reference are typically on the

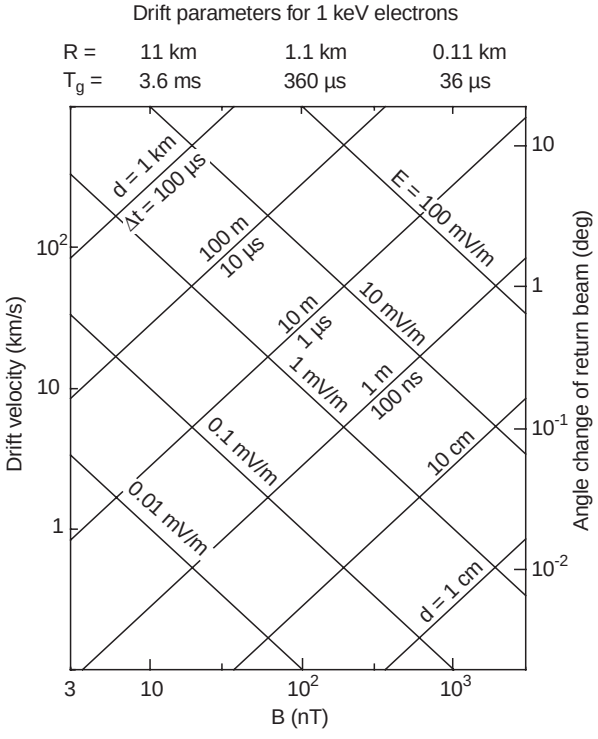

Fig. 2. Key parameters for the EDI technique for 1 keV electrons, plotted versus magnetic field **B** and the $\mathbf{E} \times \mathbf{B}$ drift velocity. *Lines* of constant drift-step **d** and electric field **E** are marked

order of 1 m, which is ideal for triangulation with baselines on the order of the spacecraft diameter.

An important feature of EDI is that the technique is largely independent of the orientations of the electric and magnetic fields with respect to the spacecraft. This is an inherent difference between the EDI and double-probe measurements of electric fields. EDI is sensitive to the two components of the **E** in the $\mathbf{B}_\perp$ plane, while the double-probe technique is most sensitive to the components in the satellite spin plane. Thus while EDI does not measure the component of **E** parallel to **B**, it measures both perpendicular components without regard to the angle of **B** with respect to the spin axis.

3 Equator-S EDI observations

We examine five intervals in late March and April, 1998, when Equator-S apogee was in the early-morning sector. During this period the satellite was operated occasionally in high-rate telemetry for approximately one-hour periods while traversing outbound orbital legs, at geocentric distances of approximately 5–6 R_E. The high-rate intervals are chosen because this telemetry includes supplementary data that enable more complete validation of the results. We present here results from five passes for which high-rate EDI data are available, as summarized in Table 1.

Figure 3 illustrates EDI detection of the returning beam during a 4-s period on April 28. Subscripts 1 and 2 in the figure panel labels denote data from each of the two EDI detectors. The panels labeled "Max1" and "Max2" show the detected counts in the onboard correlator channel having the maximum signal. These are the counts during 1 ms accumulation intervals, sampled by telemetry every 16 ms. The periods of beam hits on the detector are clearly evident as count levels of several hundred, compared to the ambient background levels of 20–50. The small panel labeled "MaxCh" indicates the number of the correlator channel (0–15) that received the maximum counts. When the beam is detected, the correlator hardware attempts to adjust its time delays so that the maximum counts remain in channel 7. This correlator tracking feature is used primarily for the time-of-flight measurements (see Paschmann *et al.*, 1999). The panels labeled "s2b" show the derived signal-to-noise ratio squared, where "noise" is the square root of the ambient background counts. This quantity is calculated from comparison of counts in the maximum correlator channel with those in another channel (Vaith *et al.*, 1998). Since s2b is calculated independently for each sample period, it can be used to identify beam hits during periods of rapidly changing ambient background fluxes. The s2b parameter is used by EDI as part of the beam recognition algorithm and also as part of the instrument's onboard control of beam current, detector-optics state, and other operational parameters. Finally, the panels labeled "q" are beam quality indices, which are used to select data in the triangulation calculations. The quality of the hits is derived from a combination of the s2b parameter, a threshold on the "Max" counts, and a requirement that the "Max Channel" is channel 7 $\pm$ 1. This combination of conditions can be set to eliminate false beam identifications very effectively. The quality parameter has 4 values, 0–3, and is plotted upward from the center of the figure for detector 1, and downward from the center for detector 2.

Table 1. Periods of inner-magnetosphere EDI high-rate data from March 25 through the end of the mission

Date	UT	R (R_E)	LT
25 March 98	21:53–22:46	5.0–6.4	01:48–02:26
02 April 98	08:17–08:59	5.0–6.1	01:22–01:54
06 April 98	01:33–02:12	5.1–6.1	01:33–01:41
13 April 98	11:54–12:36	5.0–6.1	00:45–01:17
28 April 98	08:43–09:25	5.0–6.1	23:56–00:29

During the 4-s interval shown in Fig. 3, which is typical for the periods presented here, the beam is aimed successfully to hit the detector somewhat less than half of the time. The gap between beam acquisitions is often on the order of 1 s, with periods of tracking, or nearly continuous beam re-acquisition lasting of the order of 1/2 s. The tracking duty cycle will be improved significantly for Cluster with a modified beam recognition algorithm that we have tested using the Equator-S data. We address beam acquisition and tracking issues in more detail following the discussion of Fig. 4.

The triangulation measurements for the 4-s period of Fig. 3 are illustrated for 1-s intervals in Fig. 4. The format of each panel is very similar to Fig. 1, except rather than showing only a single hit from each gun, all high-quality ($q = 3$) hits during the 1-s interval are shown. The plane of the figure is perpendicular to the ambient magnetic field (the $\mathbf{B}_\perp$ plane), with the virtual detector at the center of the figure. The X-axis is the line in the $\mathbf{B}_\perp$ plane closest to the Sun direction, as indicated by the small symbol at the end of the axis, and the magnetic field direction is out of the page. As the satellite spins, the positions of the guns with respect to the detector, projected into $\mathbf{B}_\perp$ plane, sweep out an ellipse represented in the figure by the gray area. During this interval, the angle between **B** and the spacecraft spin axis is 66°, as noted at the bottom of Fig. 3. For each hit that satisfies the $q = 3$ constraints, the gun's firing position is marked with a symbol and the firing direction is plotted as a line through the gun position. Triangles are plotted for beams fired from gun 2 to detector 1, and asterisks for beams fired from gun 1 to detector 2. For a given hit, one knows that the target (the tail of the drift step vector in Fig. 1) is somewhere along the electron trajectory that passes through the gun at the proper angle. Because there is no way of knowing, *a priori*, whether the target is located before or after the gun position on this trajectory, the beam is plotted as a line extending both forward and backward from the gun. In the regime of these measurements the gyro radius for 1 keV electrons is on the order of 1 km, so the use of straight lines for the trajectories is a very good approximation on the scale of these figures.

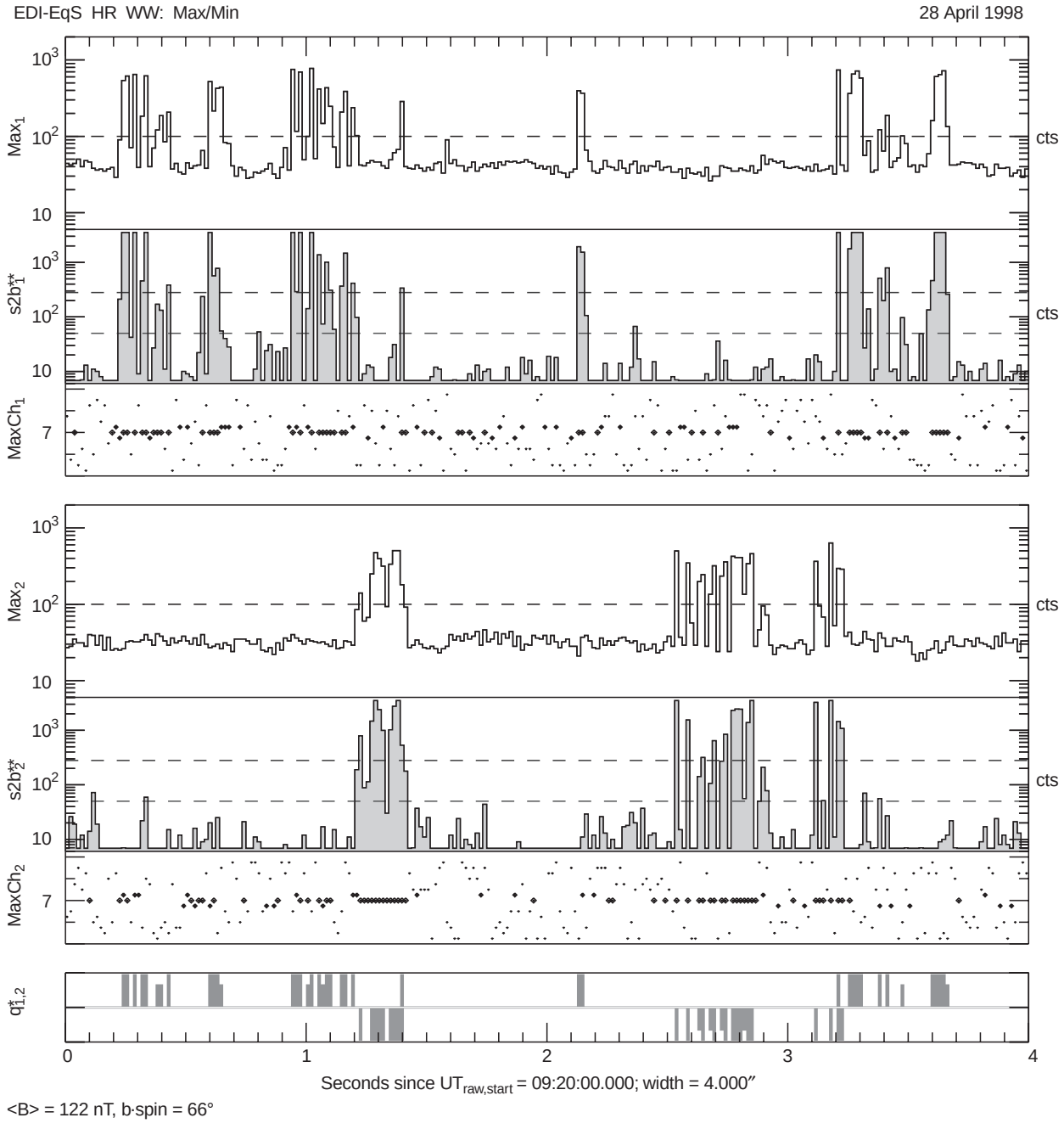

Fig. 3. EDI-detected signals, during a 4-s period on April 28, 1998, for detectors 1 and 2 (*subscripts*). "*Max*" shows the detected counts in the correlator channel with the highest counts during a 1 ms period (sampled at 16 ms intervals). "*s2b*" is a derived indication of signal (beam electrons) strength compared to the background (ambient electrons). *MaxCh* shows which of the 15 correlator channels had the maximum counts. *Bottom panel* (*q**) shows the calculated beam "quality" level, ranging from 0–3. Quality is plotted from the center of the panel, upward in the upper portion for Detector 1, and downward in the bottom portion for Detector 2

In the absence of time variations, and with perfectly measured firing angles, the intersection of any pair of beams determines the position of the tail of the drift step vector by triangulation, as shown in Fig. 1. In the extreme of a highly varying environment, the two hits must be nearly simultaneous to avoid serious errors in triangulation. However, in many cases the time variation over the time scale of spacecraft rotation is relatively small. In this situation, it is useful to display all hits over an extended period. When data are used from a significant fraction of a spacecraft spin, the changing gun position provides a variety of baselines, frequently allowing triangulation with data from only one gun. If a consistent beam intersection is obtained during such an extended period, then one has fairly high confidence that time variations were small during the interval.

From inspection of the four 1-s intervals in Fig. 4 it is evident that the time variation during this period is not appreciable. While there is some spread in the beam

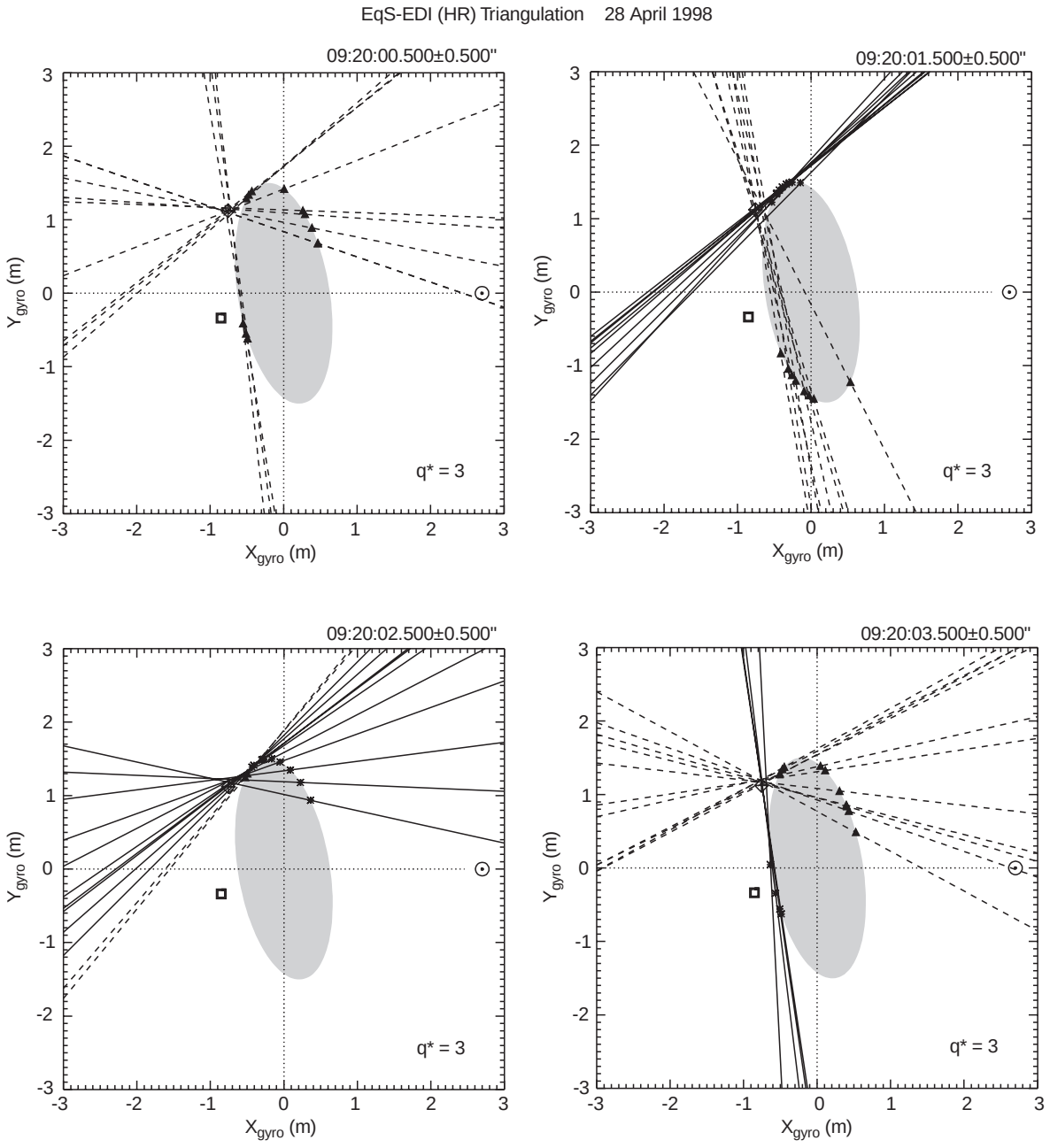

Fig. 4. Beam firing directions, plotted forward and backward, for all quality = 3 hits during four 1-s periods. Gun positions at the time of each hit, projected into the plane perpendicular to **B**, are shown as *triangles* and *asterisks* for the two guns. The virtual detector is at the center of the ellipse. The beam-intersection point, near the fixed-position *crossed-diamond symbol*, determines the tail of the drift-step vector, as indicated in Fig. 1. For comparison, the drift due to the spacecraft velocity over one gyro period is marked by the *square* in the *lower left quadrant*

intersections, it is quite small compared to the magnitude of the drift step. In order to compare the variations from panel-to-panel, a crossed diamond symbol is plotted in the same location on each plot, very near the beam intersection in the upper left panel.

The electron drift velocity in the spacecraft frame of reference can be estimated immediately from plots such as Fig. 4. For this example, the drift step, defined as the vector from the beam intersection to the center of the figure, has a magnitude of approximately 1.3 m. In a magnetic field of 122 nT, corresponding to a gyro period of about 0.3 ms, the calculated drift velocity is 4.3 km/s. The drift direction is approximately 60° from sunward. For comparison, the drift contribution due to the spacecraft velocity is marked by the square, indicating the spacecraft motion during one gyro period. (If the plasma's only motion in the spacecraft frame were due to the spacecraft's velocity, then the beams would intersect at the square).

Before proceeding to examine the results of the triangulation analyses, we discuss briefly the non-tracking (no return beam) periods that are seen in Figs. 3 and 4. While there are a number of adjustable parameters in the EDI beam control software that can affect beam

acquisition and tracking, there were two significant factors that limited the capability of EDI on Equator-S. First, during the abbreviated Equator-S mission the satellite spin axis was in the process of being rotated to its final orientation via magnetic torquing at perigee. Operation of the magnetic torquer coils induced a residual magnetic moment in the spacecraft, which at the location of the scientific magnetometer accounted for a magnetic field of up to several nT. Because magnetic torquing was performed during most perigees, with differing residual magnetization, it was typically not possible to prepare and upload up-to-date magnetic offsets for the EDI Controller to use in accurate onboard determination of the magnetic field direction. As an example, during the April 28 period shown in Figs. 3 and 4, unoptimized magnetic offsets in the onboard software were responsible for a spin-dependent error in the magnetic field direction of approximately 0.5°. An error of this size can significantly impact the critical capability of firing the beam in the $\mathbf{B}_\perp$ plane. This is one factor in the spin-phase dependence of the hits in Fig. 4. It is important to note that for a spacecraft that is not actively using magnetic torquing, such as Cluster, the effects of a residual magnetic moment are quickly and easily accounted for in the onboard software. Indeed, as described by Paschmann *et al.* (1999), the EDI time-of-flight measurements provide an excellent method for determining the spin-axis component of the offset, which can be difficult to ascertain otherwise.

The second major factor contributing to the relatively long periods between beam acquisitions arises from the beam recognition algorithm that was used on Equator-S. In analysis of the Equator-S data we have discovered that our beam recognition algorithm was overly sensitive to false positives, due to improperly handled counting statistics at moderate- to low-count rates. This led to sporadic false beam identifications in the ambient background fluxes which would delay the beam acquisition sequence. These false identifications are easily avoided in the ground data analysis and by a corrected onboard algorithm that we have developed and tested using Equator-S data. We expect the new algorithm to greatly reduce false beam identifications on Cluster.

The drift velocities presented here were derived using triangulation plots similar to Fig. 4. For each 8-s interval, a complete sequence of triangulation plots were made, with time widths ranging from 0.1 to 1 s. We examined the plots to determine an unambiguous beam intersection with at least three beams, such as displayed in the upper left panel of Fig. 4. Within each 8-s period, one stable intersection was identified and marked, and all the relevant data stored in a file. In cases where there was no well-defined beam intersection, no data were stored. When significant target motion occurred within the 8-s interval, a single measurement was chosen based on having an unambiguous beam intersection within the time sub-interval. Thus while there is often significant time variation within an 8-s interval, each sample represents a well-defined measurement.

Figure 5 shows the triangulation results for the April 28 high-rate pass in a frame co-rotating with the earth. The top panel shows the electric-field magnitude corresponding to the measured drift velocity. The middle panel shows the angle of the drift projected into the X-Y_{GSE} plane (0° is sunward). The bottom panel shows the Y_{GSE} component of the electric field, which is chosen to compare with other studies as described later. Although the choice of the co-rotating frame is somewhat arbitrary, it is useful for comparison with other published results. Also, because the contribution of co-rotation can be significant at these altitudes, the co-rotating frame yields lower average drift velocities than the non-rotating frame for the periods in this study. The two data gaps (08:59–09:02 and 09:07–09:16) are intervals when the EDI telemetry was allocated to testing special instrument modes, so that triangulation data are not available. These diagnostic tests were scheduled for several minutes of each high-rate pass during Equator-S operations in March and April.

The electric fields presented here have not been corrected for $\nabla\mathbf{B}$ drifts, which are included in the drift step that is measured by EDI. While the instrument is designed to use different beam energies for separating the (energy-independent) $\mathbf{E}\times\mathbf{B}$ drift from the (energy-dependent) $\nabla\mathbf{B}$ drift, this mode was not operated on

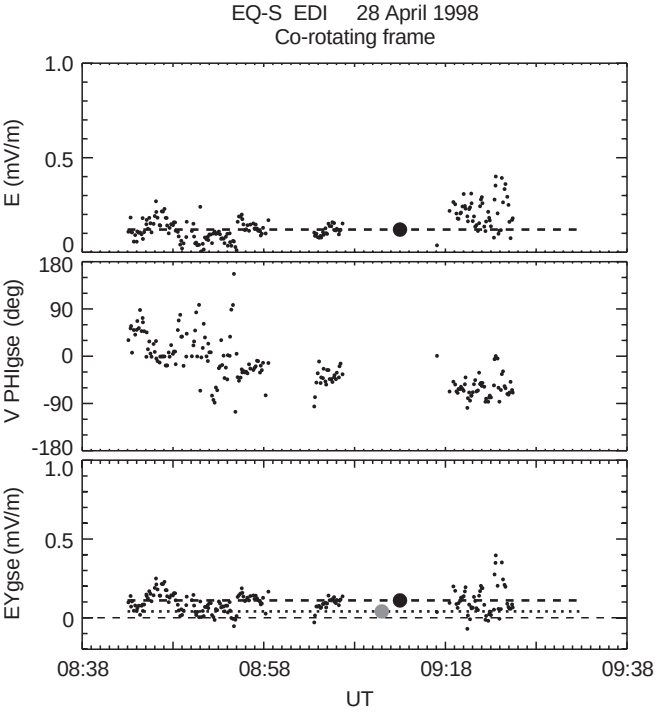

Fig. 5. EDI triangulation results for April 28, 1998, in the frame co-rotating with the Earth. The electric-field magnitude (*top*), drift direction in the X-Y_{GSE} plane (*center*), and the Y_{GSE} component of the electric field are shown by *dots* at approximately 8-s sampling. The *dashed black line* (*top* and *bottom*) represents the mapped Weimer model for a 40-min solar wind average. The *dotted line* (*bottom*) are Rowland and Wygant (1998) CRRES results, parameterized by K_p. Missing data (08:59–09:02 and 09:07–09:16), are periods when EDI triangulation telemetry are unavailable due to testing of other instrument modes

Equator-S. The magnitude of the $\nabla\mathbf{B}$ drift can be estimated by considering an equatorial dipole magnetic field at geocentric radii between 5 and 6 R_E. For 1 keV electrons, the gradient drift in this field would be 0.38 and 0.54 km/s in the eastward direction for radii of 5 and 6 R_E respectively. In the absence of a $\nabla\mathbf{B}$ correction, this drift could be misinterpreted as arising from an $\mathbf{E}\times\mathbf{B}$ drift. For the same dipole magnetic field, these velocities would correspond to radially-inward-directed electric fields of 0.093 and 0.078 mV/m.

The triangulation data in Fig. 5 show a relatively weak electric field, with an average magnitude of approximately 0.1 mV/m, and variations of a similar magnitude on a time scale of tens of seconds or less. The drift direction is quite variable, but is typically within about $\pm 90°$ of sunward. This drift is comparable in magnitude to that expected from the $\nabla\mathbf{B}$ drift, but in approximately the perpendicular direction. Thus a $\nabla\mathbf{B}$ correction would be significant quantitatively, but not qualitatively. In particular, the clear trend of drift direction in the GSE X-Y plane, seen in the middle panel of Fig. 5, is not altered significantly by the $\nabla\mathbf{B}$ drift. Using a dipole magnetic field model, the drift angle at the beginning of the pass changes from approximately 45° to a $\nabla\mathbf{B}$-corrected value of 65°, while at the end of the pass the direction changes from about −60° to a corrected value of −45°.

In order to provide a comparison with the EDI measurements, we use results from empirical studies by Weimer (1995, 1996) and Rowland and Wygant (1998). Weimer's ionospheric-potential model (1995, 1996) is parameterized by solar wind and IMF conditions, which we obtained from the Wind MFI and SWE instruments for this study. The solar-wind parameters used as inputs were averaged over a 40-min period, as were the solar-wind data in Weimer's study. These parameters were time-shifted for the transit period from Wind to the earth, and shifted by another 40 min to approximate the time for convection fields to be established in response to solar-wind conditions. The resulting Weimer potential model was then mapped to the location of Equator-S using the Tsyganenko-96 magnetic field model (Tsyganenko, 1996). The magnitude of the mapped Weimer electric field is indicated in the top panel by the large black dot and the dashed line. The Y_{GSE} component of the model is shown in the bottom panel with the same symbol. It is important to note that the Weimer model is derived from ionospheric data having a time scale of a low-altitude satellite pass, and is parameterized by 40-min time-averaged solar-wind inputs. It is not intended to reproduce the short-term variations that are apparent in the EDI data and are due at least in part to local wave-fields. However, the model does provide an estimate of the background "steady state" field for comparison with the EDI results. Indeed the baseline of the EDI fluctuating field measurements shown in Fig. 5 agrees well with the Weimer model value.

A second comparison for the EDI results can be made with averaged data from the CRRES double-probe instrument. Rowland and Wygant (1998) used 10 months of CRRES measurements to determine the average Y_{GSE} component of the electric field as a function of L and K_p, for local times between 1200 and 0400. The bottom panel of Fig. 5 shows the Rowland and Wygant (1998) result, for the K_p interval containing the EDI measurements, as a gray circle and dotted line. As with the Weimer model, this is an average value, meant to provide a reference for the "DC" component of the electric field.

The interplanetary and geomagnetic conditions used as inputs for the two empirical models, and the Tsyganenko (1996) mapping field, are shown in Table 2. All five cases are relatively quiet geomagnetically, with a maximum K_p of 2−.

Figures 6–9 show EDI results for the four other high-rate passes in the same format as Fig. 5. As before, values from the Weimer model (1995, 1996), and the Rowland and Wygant (1998), CRRES study are shown for comparison baselines. The most notable differences between the April 28 case discussed previously and the four other cases are the degree of variability in the magnitudes and directions of the fields. April 28 shows relatively small fluctuations in both magnitude and direction; April 2 has large directional variations but a fairy stable magnitude; April 13 has a more stable direction but variable magnitude; while March 25 and April 6 are quite variable in both parameters. These differences represent the diversity of physical processes contributing to the electric-field environment even in relatively quiet times. Considering that the Weimer (1995, 1996) and the Rowland and Wygant (1998) model values are derived from averaged data sets containing similar variability, and parameterized with a small set of inputs, the agreement with the EDI results is quite good.

The data in Figs. 5–9 emphasize again the large temporal variability of the convection fields that transport plasma in this region. In particular, while slowly varying, large-scale convection-field models successfully explain many aspects of transport and energization, it is clearly necessary to be aware of the highly variable nature of the convection. For example, conclusions depending on slow variations over an ion bounce-period would certainly be questionable for the cases presented here. It has been known for some time that large-scale convection surges on time scales shorter than a bounce

Table 2. Interplanetary and geomagnetic conditions. The solar wind conditions are averaged over a 40 min interval, offset from the EDI measurements as described in the text

Date	Center UT	V_{SW} (km/s)	N_P (cm^{-3})	IMF B_Y (NT)	IMF B_Z (nT)	DST	K_P
25 March 98	22:20	416	19	7	5	−46	2−
02 April 98	08:37	319	7	2	1	−16	0+
06 April 98	01:53	350	9	3	1	−9	1+
13 April 98	12:15	405	7	2	4	−17	0+
28 April 98	09:05	455	4	−2	0	−36	2−

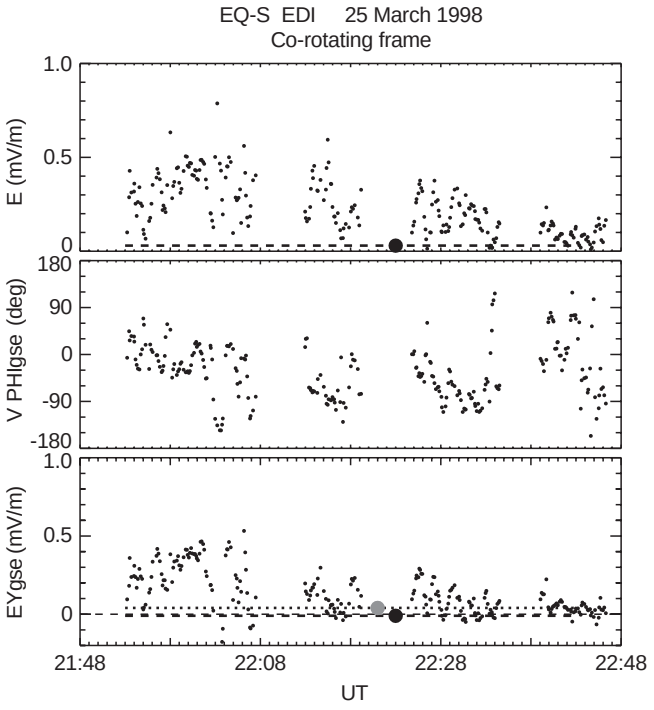

Fig. 6. March 25, 1998 measurements in the co-rotating frame. Same format as Fig. 5. Missing data (22:08–22:12, 22:20–22:24, 22:35–22:39) are gaps in the EDI triangulation telemetry during diagnostic testing

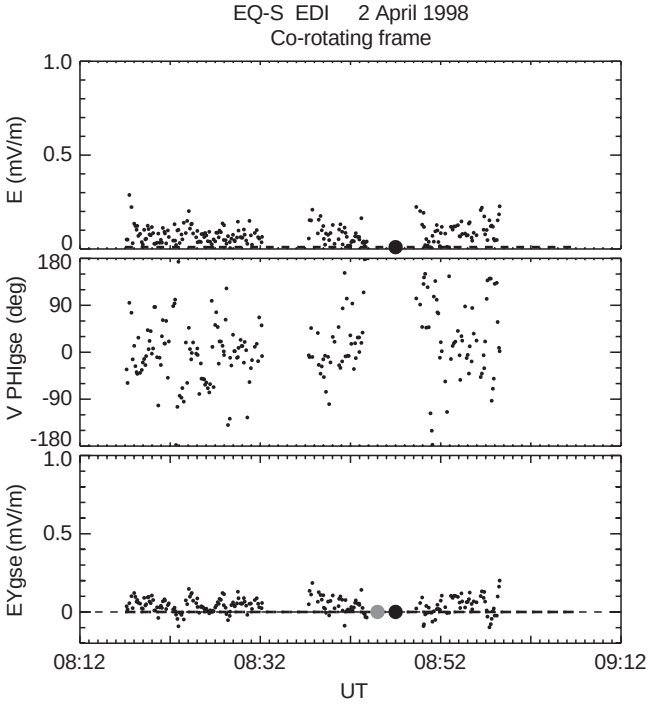

Fig. 7. April 2, 1998 measurements in the co-rotating frame. Same format as Fig. 5. Missing data (08:32–08:37 and 08:44–08:49) are gaps in EDI triangulation telemetry during diagnostic testing

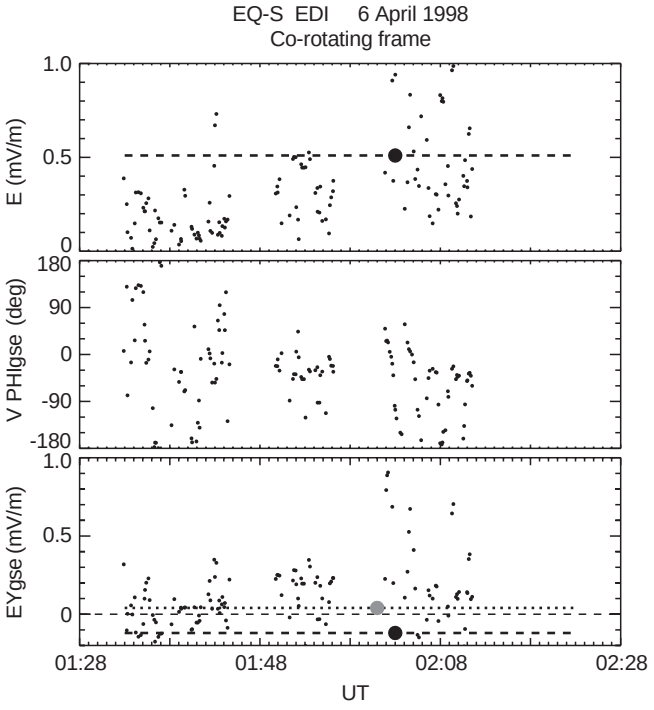

Fig. 8. April 6, 1998 measurements in the co-rotating frame. Same format as Fig. 5. Missing data (01:45–01:49 and 01:56–02:02) are gaps in EDI triangulation telemetry during diagnostic testing

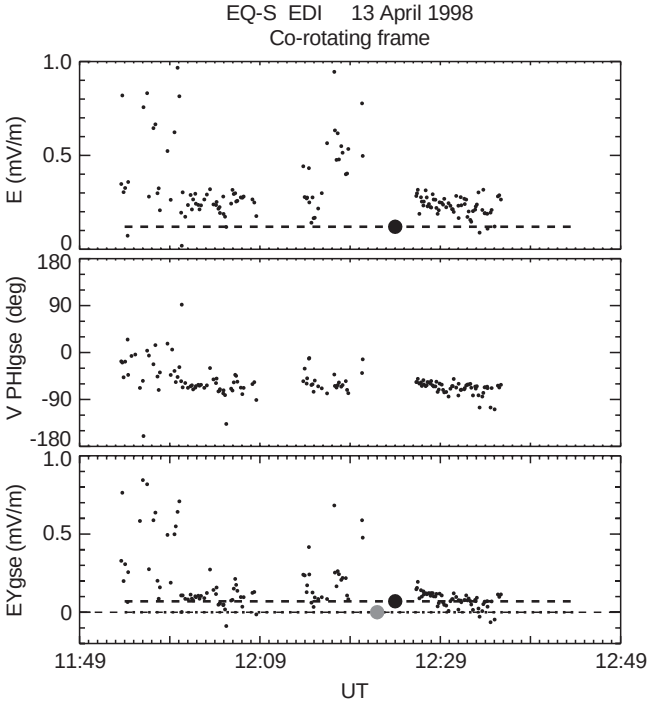

Fig. 9. April 13, 1998 measurements in the co-rotating frame. Same format as Fig. 5. Missing data (12:09–12:13 and 12:20–12:26) are gaps in EDI triangulation telemetry during diagnostic testing

period can play a significant role in determining the ion pitch-angle structure in the vicinity of geosynchronous orbit (Quinn and Southwood, 1982; Mauk, 1986). It may be that electric field variations that violate the second adiabatic invariant have an important effect during even the quietest times, such as presented in this study. We look forward to studying the spatial scale of these electric-field variations with the Cluster spacecraft.

In an effort to identify possible electromagnetic-wave sources of the electric-field variations, we have examined the Equator-S magnetic-field data during the five

intervals at highest resolution. The magnetic field for all five cases is extremely quiet, varying smoothly in both magnitude and direction. The electric-field variations seen in Figs. 5–9 are apparently electrostatic, except for a possible electromagnetic contribution at frequencies well above 50 Hz, which would not be visible to the magnetometer.

4 Summary

Equator-S EDI measurements in the 5–6 R_E, post-midnight region demonstrate the instrument's capability to measure accurately the quiet-time ~0.1 mV/m fields in this region of space. During five 1-h passes in geomagnetically quiet times, convection in the frame co-rotating with the Earth was, on average, in the sunward direction, but with variations in direction of approximately $\pm 90°$ over time scales of a few minutes or less. The field magnitudes in this frame were a few tenths mV/m, with variations of approximately 100% over periods of <1 min. Comparison of the EDI measurements with the "steady state" empirical values from the Weimer (1995, 1996) ionospheric model and the Rowland and Wygani (1998) CRRES results yield reasonable agreement, although, as noted, the short-term temporal variations are comparable to or greater than the "DC" level. The large variability of the electric fields in this region of space is presumably an important factor in properly treating plasma convection and energization in this region of space, and its injection into the inner magnetosphere.

The Cluster flight of EDI will benefit greatly from our Equator-S experience, and we expect large improvements in the instrument's beam-tracking duty cycle. Without the magnetic torquing that was ongoing throughout the lifetime of Equator-S, we will be able to compensate effectively for any residual spacecraft magnetic moments or other offsets in the onboard magnetic field. This will allow accurate firing of the beam in the $\mathbf{B}_\perp$ plane, which is critical for finding and tracking the beam. In addition, the improved beam recognition algorithm that has been developed and tested with Equator-S data will significantly reduce the number of false hits, thus improving tracking and beam acquisition. Finally, on Cluster we will operate the instrument using two different beam energies, allowing for a model-independent subtraction of $\nabla\mathbf{B}$ drifts.

Acknowledgements. The authors would like to thank the many people who have made the EDI experiment possible through years of development, testing, and operational support. In particular, EDI on Equator-S owes great thanks to B. Briggs, R. Frenzel, S. Frey, W. Göbel, J. Googins, G. King, S. Longworth, R. Maheu, F. Melzner, U. Pagel, P. Parriger, D. Simpson, K. Strickler, and C. Young. We are grateful to the Equator-S spacecraft team, including H. Höfner, F. Melzner, G. Needell, P. Parriger, and J. Stöker; and the mission operations team at DLR/GSOC, especially A. Braun and T. Kuch. We thank R. Lepping and K. Ogilvie for use of the Wind MFI and SWE key parameter data used in this study. The authors thank the referee for several helpful comments. This work was supported by NASA grant NAG5-6935 and the German Space Agency DLR, through grant 50OC89043. The Equator-S project was supported through DLR grant 50OC94024.

The Editor in-Chief thanks K. Torkar for his help in evaluating this paper.

References

Baumjohann, W., and G. Haerendel, Magnetospheric convection observed between 0600 and 2100 LT: solar wind and IMF dependence, *J. Geophys. Res.*, **90,** 6370, 1985.

Baumjohann, W., G. Haerendel, and F. Melzner, Magnetospheric convection observed between 0600 and 2100 LT: variations with Kp, *J. Geophys. Res.*, **90,** 393, 1985.

Mauk, B. H., Quantitative modeling of the "convection surge" mechanism of ion acceleration, *J. Geophys. Res.*, **91,** 13 423, 1986.

Maynard, N. C., T. L. Aggson, and J. P. Heppner, The plasmaspheric electric field as measured by ISEE I. *J. Geophys. Res.*, **88,** 3991, 1983.

McIlwain, C. E., Plasma convection in the vicinity of the geosynchronous orbit, in *Earth's Magnetospheric Process*, Ed, B. M. McCormac 268, 1972.

Melzner, F., G. Melzner, and D. Antrack, The Geos electron beam experiment, S 329, *Space Sci Instru.*, **4,** 45, 1978.

Paschmann, G., F. Melzner, R. Frenzel, H. Vaith, P. Parrigger, U. Pagel, O. H. Bauer, G. Haerendel, W. Baumjohann, N. Sckopke, R. B. Torbert, B. Briggs, J. Chan, K. Lynch, K. Morey, J. M. Quinn, D. Simpson, C. Young, C. E. McIlwain, W. Fillius, S. S. Kerr, R. Maheu, and E. C. Whipple, The electron drift instrument for Cluster, *Space Sci. Rev.*, **79,** 233, 1997.

Paschmann, G., C. E. McIlwain, J. M. Quinn, R. B. Torbert, and E. C. Whipple, The electron drift technique for measuring electric and magnetic fields, in *Measurement Techniques in Space Plasmas: Fields*. Geophysical Monograph 103, Am. Geophys. Union, 1998.

Paschmann, G., N. Sckopke, H. Vaith, J. M. Quinn, O. H. Bauer, W. Baumjohann, W. Fillius, G. Haerendel, S. S. Kerr, C. A. Kletzing, K. Lynch, C. E. McIlwain, R. B. Torbert, and E. C. Whipple, EDI electron gyro time measurements on Equator-S, *Ann. Geophysicae*, this issue, 1999.

Rowland, D. E., and J. R. Wygant, Dependence of the large-scale, inner magnetospheric electron field on geomagnetic activity, *J. Geophys. Res.*, **103,** 14 959, 1998.

Quinn, J. M., and D. J. Southwood, Observations of parallel ion energization in the equatorial region, *J. Geophys. Res.*, **87,** 10 536, 1982.

Tsyganenko, N. A., Effects of the solar wind conditions on the global magnetospheric configurations as deduced from data-based field models, *Proc. Third International Conference on Substorms* (ICS-3), *Eur. Space Agency Spec. Publ.*, **SP-389,** 181, 1996.

Vaith, H., R. Frenzel, G. Paschmann, and F. Melzner, Electron gyro time measurement technique for determining electric and magnetic fields, in *Measurement Techniques in Space Plasmas: Fields*, Eds. Pfaff, Borovsky, and Young *Geophysical Monograph* **103,** 47, American Geophysical Union, 1998.

Weimer, D. R., Models of high-latitude electric potentials derived with a least error fit of spherical harmonic coefficients, *J. Geophys. Res.*, **100,** 19 595, 1995.

Weimer, D. R., A flexible, IMF dependent model of high-latitude electric potentials having "space weather" applications, *Geophys. Res. Lett.*, **23,** 2549, 1996.